

# Platinum-Palladium Core–Shell Nanoflower Catalyst with Improved Activity and Excellent Durability for the Oxygen Reduction Reaction

Altamash M. Jauhar, Fathy M. Hassan, Zachary P. Cano, Md Ariful Hoque, and Zhongwei Chen\*

In this work, highly active and stable platinum–palladium core–shell nanoflowers supported on sulfur-doped graphene (PtPd-NF/SG) with a polyol reduction method are synthesized. Platinum is decorated on palladium seeds to form core–shell structured floral petals to improve surface activity and give high electrochemically active surface area and stability. The catalyst is deposited on sulfur-doped graphene to induce highly favorable catalyst-support interactions to ensure long-term electrochemical stability. The specific activity and mass activity of the synthesized core–shell nanocatalysts are 3.2 and 4.7 times higher than commercial Pt/C toward oxygen reduction reaction, respectively. After 10 000 testing cycles, the mass and specific activity of the catalyst is  $\approx$ 25 and  $\approx$ 18 times higher than the Pt/C benchmark catalyst, respectively. The enhanced electrochemical activity and excellent stability of PtPd-NF/SG can be attributed to the 2D core–shell nanoflower structure, weak binding of hydroxyl groups to the platinum metal deposited on palladium, and robust sulfur-doped graphene support.

Platinum (Pt) is the most critical component of the catalysts used to facilitate the oxygen reduction reaction (ORR) in polymer electrolyte membrane fuel cells (PEMFCs). While it offers a higher catalytic activity for ORR than any other metal, the sluggish ORR kinetics, low durability, and persistently high price of Pt limits large scale commercialization of PEMFCs. At present, desired fuel cell performance and stability under simulated drive cycles requires significantly higher Pt loading compared to the Department of Energy (DOE) guidelines.<sup>[1]</sup> Therefore, reducing Pt loading and improving durability is a central focus of industrial and academic research. At cathode in PEMFCs, in the first step oxygen gas is adsorbed at the active sites, where it reacts with an electron and proton to form OOH species. This oxygen group further reacts with protons and electrons and leads to the formation of H<sub>2</sub>O. If oxygen species

are strongly adsorbed, this reduces the availability of active sites and negatively affects ORR activity. The addition of secondary metals such as palladium (Pd) to Pt can change the d-band center, surface atomic arrangement, and decrease chemisorption of oxygen-containing species (mostly hydroxyl ions), thus positively impacting the ORR kinetics.<sup>[2]</sup> However, the binding energy of oxygen on Pd is 0.4 eV higher than Pt, which results in lower ORR activity of Pd and highlights the importance of limiting surface exposure of pure Pd in Pt–Pd catalysts. It has also been recognized that strain development in Pt-based materials can decrease the binding affinity of oxygen groups. Therefore, core–shell nanostructure catalysts such as Pt–Pd structures can be engineered to create internal strain to improve ORR activity.<sup>[3]</sup> Pt–Pd catalysts

can also exhibit better durability than pure Pt, as addition of Pd could prevent the corrosion of Pt by sacrificing itself to provide cathodic protection.<sup>[4]</sup>

Careful design of Pt nanostructures is another effective way to modulate the activity and protect against loss of electrochemically active surface area (ECSA).<sup>[5–7]</sup> Pt-based catalysts currently used in PEMFCs consist of 2–5 nm nanoparticles having ill-defined shapes and facet structures.<sup>[8]</sup> 0D Pt/C nanoparticles, while offering high surface area, have diminished electrocatalytic activity due to their significant number of defect sites, lattice boundaries, and low atomic coordination on the surface. During PEMFC operation, which is typically in the voltage range of 0.8–0.9 V or above, Pt nanoparticles are also susceptible to agglomeration, dissolution, and Ostwald ripening due to their high surface energy and carbon support corrosion, which ultimately results in detachment of Pt nanoparticles from the support and an ensuing decline in performance.<sup>[9–11]</sup> Therefore, Pt particle properties and the interaction between Pt and the support material play an important role in the catalyst's activity and stability. 2D Pt nanostructures such as plate or flower-like structures can be engineered to improve durability by growing onto stable nanostructured support materials such as graphene or carbon nanotubes.<sup>[11–13]</sup> When compared with commercial carbon black, graphene possesses an incredible improvement in chemical, mechanical, and electrical properties due to its

A. M. Jauhar, Dr. F. M. Hassan, Z. P. Cano,  
 Dr. M. A. Hoque, Dr. Z. Chen  
 Department of Chemical Engineering  
 University of Waterloo  
 200 University Ave. W, Waterloo, Ontario N2L 3G1, Canada  
 E-mail: zhchen@uwaterloo.ca

The ORCID identification number(s) for the author(s) of this article can be found under <https://doi.org/10.1002/admi.201701508>.

DOI: 10.1002/admi.201701508

unique 2D  $sp^2$  hybridized carbon structure.<sup>[11–13]</sup> Traditional carbon can be heated to high temperatures ( $\approx 1000$  °C), leading to lattice rearrangement and an increase in graphitic nature of the material. Graphitization produces a highly resistant material to oxidation and carbon corrosion. To further improve performance, several studies have incorporated heteroatoms doping of graphene as an efficient way to tune intrinsic properties, which is helpful in improving electrocatalyst activity and stability.<sup>[12,14]</sup>

Recent research efforts have been focused on the development of less expensive and improved electrochemically active catalysts such as advanced Pt alloys, nonprecious metal catalysts, and core–shell catalysts. Among these, core–shell structure catalysts consisting of a thin layer of Pt deposited on low cost seed material have attracted considerable attention.<sup>[4,6,15,16]</sup> Deposition of an ultrathin Pt shell on Pd offers a great opportunity to enhance catalytic activity and durability while reducing its loading.<sup>[15,17]</sup> However, nonuniform deposition of the Pt shell and long-term durability at high potential range is still a problem with core–shell structures. This motivated us to carefully design a Pt–Pd electrocatalyst and integrated uniquely carbon support to improve durability and achieve the DOE targets. To improve Pt-based ORR activity and more importantly long-term durability, herein, we report

a Pt–Pd core–shell nanoflower supported on sulfur-doped graphene (SG) with improved activity and excellent durability. The 2D nanoarchitecture of the core–shell nanoflowers provides enhanced surface activity and improved electron kinetics, while sulfur atoms doped on graphene support provide a strong anchor for the nanoflowers through tethering behavior, leading to excellent durability under very aggressive test conditions.<sup>[18]</sup> The electrochemical activity and stability of the prepared electrocatalyst was investigated. Enhancement in electrochemical activity can be attributed to the nanoflower core–shell Pt–Pd nanostructure and weak –OH binding to Pt in comparison to Pd. The morphology of the catalyst was responsible for high ECSA, while its core–shell structure and the interaction between the catalyst and highly robust SG facilitate long-term stability to high potential cycling.

The catalyst synthesis procedure is demonstrated in Figure 1, and the detailed synthesis route and reaction mechanism is provided in Figure S1 (Supporting Information). Pd nanoparticle seeds were selectively synthesized through manipulation of the reduction kinetics of the polyol process,<sup>[19,20]</sup> by reducing Pd salt ( $PdCl_4^{2-}$ ) with diethylene glycol and polyvinyl pyrrolidone (PVP) (Figure 1a,b). Generally, metallic particles are thermodynamically favored to form into bulk shapes to lower surface-free energies. The addition of PVP reduced the reduction rate

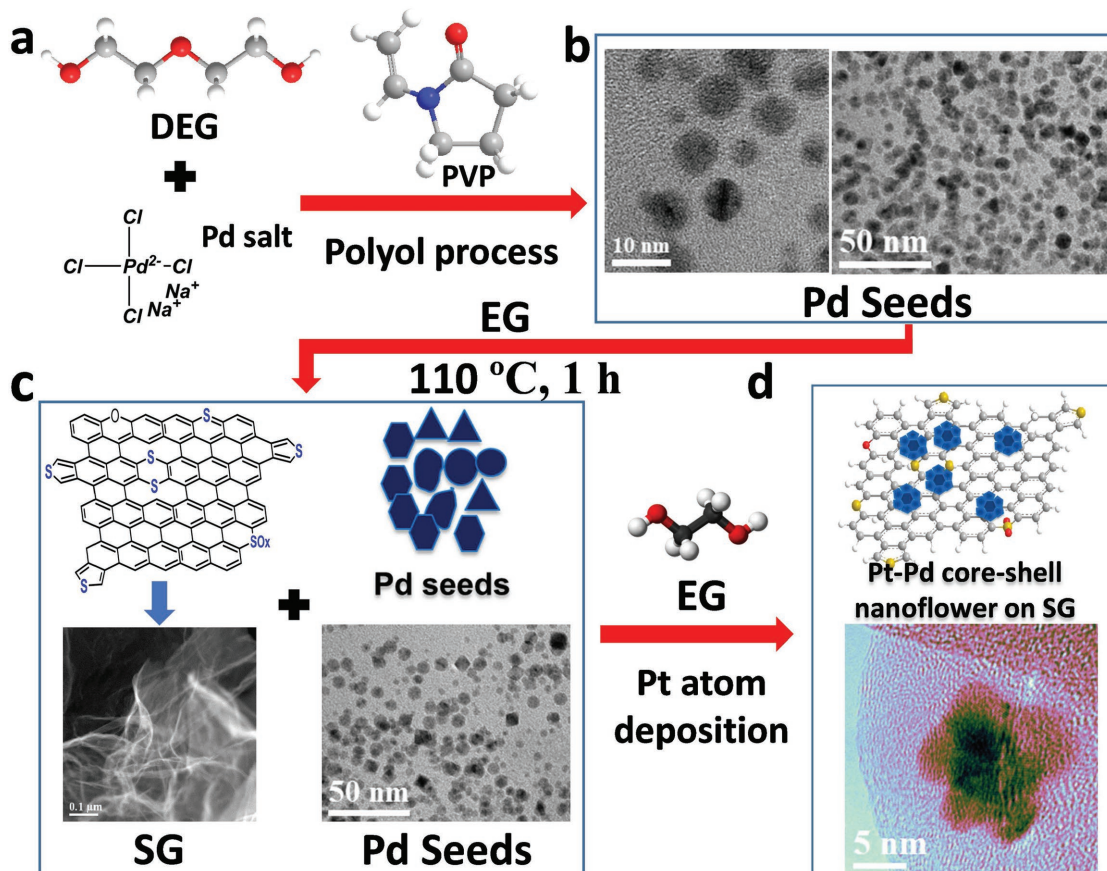


**Figure 1.** Schematic illustrations of synthesis of  $Pt_xPd_y$ -NF/SG core–shell nanoflower (here x, y subscript represents atomic percentage) synthesis. Synthesis followed as Pd seed synthesis, Pd deposition on SG, with in situ Pt deposition on Pd seed. Here light blue (Pt), dark blue (Pd), and yellow (S) in Pt–Pd core–shell nanoflower.

and allowed the nucleation and growth to be kinetically controlled,<sup>[24]</sup> which prevented the nanoparticles from growing too large and agglomerating. Separately, graphene oxide and phenyl disulfide (PDS) were mixed and subjected to a thermal shock (1000 °C) and quenching process to synthesize SG, which exhibits a multilayer sheet-like structure (Figure 1c). The Pd seeds, which served as a template for Pt deposition, were well dispersed and attached onto SG (Figure 1c) in a solution of ethylene glycol, PVP, potassium bromide (KBr), and ascorbic acid and heated at 110 °C for an hour. The final product, Pt–Pd core–shell nanoflowers on SG (Pt–Pd NF/SG) (Figure 1d), was synthesized by an *in situ* continuous feeding method. A syringe pump was used to introduce a solution of Na<sub>2</sub>PtCl<sub>6</sub> · 6H<sub>2</sub>O and ethylene glycol (EG) into the growth solution used for attaching Pd seeds on SG. Addition of the Pt precursor into the growth solution caused immediate reduction to metallic Pt by ascorbic acid and EG. A low injection rate was used to maintain low concentrations of Pt, thus preventing self-nucleation and agglomeration while promoting highly dispersed Pt deposition.

The transmission electron microscopy (TEM) images in Figure 2a–c show well attached and dispersed nanoflowers on SG sheets. PtPd-NF/SG was synthesized with different Pt:Pd atomic ratios, with 90 at% Pt (Pt<sub>0.9</sub>Pd<sub>0.1</sub>/SG, Figure 2a–c) and 50 at% Pt (Pt<sub>0.5</sub>Pd<sub>0.5</sub>/SG), (Figure S2, Supporting Information). Pt<sub>0.9</sub>Pd<sub>0.1</sub>/SG appears well dispersed on SG (Figure 2a), and their nanoflower morphology is confirmed in the high-angle annular dark-field scanning TEM (HAADF-STEM) and high-resolution TEM (HR-TEM) images in Figure 2b,c. Energy dispersive X-ray spectroscopy (EDX) was used to detect the

distribution of elements (particularly Pt and Pd) in the material, while electron energy loss spectroscopy (EELS) was employed to detect light elements (i.e., carbon and sulfur) with high spatial resolution. EDX elemental mapping of two particles of Pt<sub>0.9</sub>Pd<sub>0.1</sub>/SG (Figure 2d) confirm the Pd core–Pt shell structural distribution of these two elements. To further confirm the core–shell structure, an EDX line scan profile of Pd (red) and Pt (black) across a Pt–Pd nanoflower is shown in Figure 2e, which displays normalized intensities of Pd and Pt. The two high-Pt intensity peaks at the sides with the high-Pd intensity peak in between indicate the presence of a Pd core and Pt shell. The size of the core and entire core–shell structure is 5–10 and 15–20 nm, respectively. The EDX spectra of sulfur, Pt and Pd in Pt<sub>0.9</sub>Pd<sub>0.1</sub>/SG and Pt<sub>0.5</sub>Pd<sub>0.5</sub>/SG are compared in Figure 2f, with the larger Pt peak in Pt<sub>0.9</sub>Pd<sub>0.1</sub>/SG and larger Pd peak in Pt<sub>0.5</sub>Pd<sub>0.5</sub>/SG indicating the successful control of the relative elements in each structure. In Figure S3 (Supporting Information), a low magnification HAADF-STEM image and corresponding EDX maps show the same Pd core–Pt shell structure across a large number of Pt<sub>0.9</sub>Pd<sub>0.1</sub>/SG particles, while sulfur is homogenously distributed across the SG sheet. Figure S4 (Supporting Information) shows a lower magnification HAADF-STEM overview of Pt<sub>0.9</sub>Pd<sub>0.1</sub> nanoflower distribution on SG, with EDX elemental mapping indicating homogenous distribution of sulfur atoms and PtPd nanoflowers across the graphene sheet. Figure 2g displays a HAADF-STEM image of Pt<sub>0.9</sub>Pd<sub>0.1</sub>/SG and associated EELS maps of sulfur and carbon. Sulfur is concentrated particularly underneath the Pt petals of the nanoflower, indicating the desirable anchoring interaction

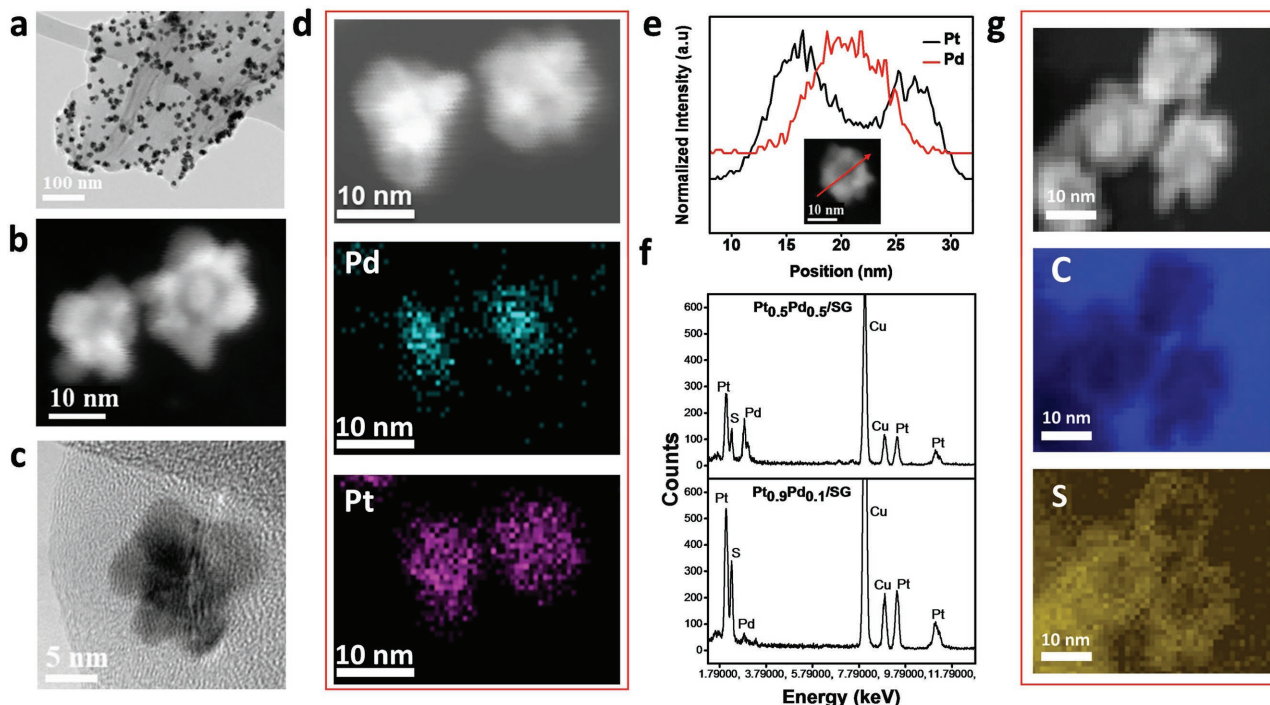


**Figure 2.** a) TEM image of Pt<sub>0.9</sub>Pd<sub>0.1</sub>/SG (Pt–Pd core–shell nanoflower). b) HAADF-STEM image of Pt<sub>0.9</sub>Pd<sub>0.1</sub>/SG Pt–Pd core–shell nanoflower. c) HR-TEM image of Pt–Pd core–shell nanoflower. d) HAADF-STEM image of two Pt–Pd core–shell nanoflower particle and their corresponding EDX maps of Pd and Pt. e) EDX line scan of profiles of Pt (black) and Pd (red) of a single Pt–Pd core shell nanoflower particle. f) EDX spectra comparison of Pt<sub>0.5</sub>Pd<sub>0.5</sub>/SG and Pt<sub>0.9</sub>Pd<sub>0.1</sub>/SG with Pt, Pd, and S peaks (Cu peaks are attributed to the TEM grid). HAADF-STEM image of Pt–Pd core–shell nanoflowers and corresponding EELS spectra of sulfur (S) and carbon (C).

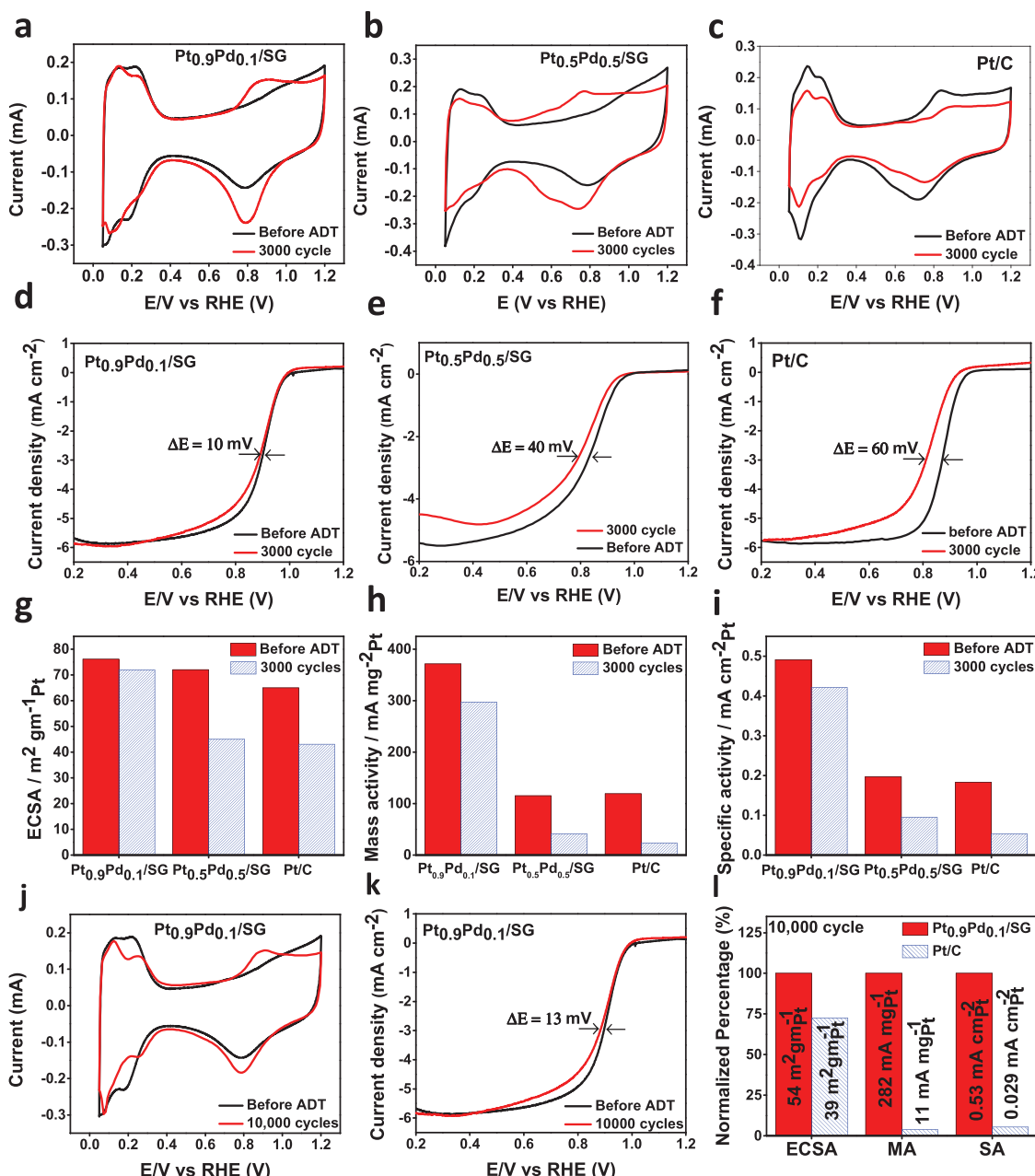
between these two elements as demonstrated in our previous works.<sup>[18,22]</sup>

Figure S5 (Supporting Information) shows that the X-ray diffraction (XRD) patterns of Pt<sub>0.9</sub>Pd<sub>0.1</sub>/SG and Pt<sub>0.5</sub>Pd<sub>0.5</sub>/SG reveal typical Pt-fcc peaks (JCPDS No. 04-0802), with diffraction pattern of Pd/SG and commercial Pt/C shown for comparison. The (111) crystal face, which delivers increased Pt mass-based ORR activity in comparison to commercial Pt/C,<sup>[23–25]</sup> is prominent in Pt<sub>0.9</sub>Pd<sub>0.1</sub>/SG and Pt<sub>0.5</sub>Pd<sub>0.5</sub>/SG relative to the other characteristic peaks. There was no elemental sulfur, indicated by the lack of characteristic sulfur peaks. Pt and Pd have the same crystal structure and similar lattice constants, which makes them difficult to distinguish in regular XRD measurements. X-ray photoelectron spectroscopy (XPS) can be used to investigate the electronic state of a catalyst material surface, which is a significant factor in the catalytic activity and durability of Pt.<sup>[26]</sup> Figure S6 (Supporting Information) displays the full XPS spectra of SG, Pd/SG, Pt<sub>0.9</sub>Pd<sub>0.1</sub>/SG, and Pt<sub>0.5</sub>Pd<sub>0.5</sub>/SG. The C1s peaks for SG are deconvoluted into separate peaks corresponding to sp<sup>2</sup> C=C (284.41 eV), sp<sup>3</sup> C-C (285.82 eV), C=O (287.90 eV), and π-π\* (290.65 eV) (Figure S7a, Supporting Information),<sup>[27–30]</sup> with the results showing that SG largely comprises sp<sup>2</sup> C=C bonds. After deposition of Pt on SG to create Pt<sub>0.9</sub>Pd<sub>0.1</sub>/SG, the C=C peak is shifted to 284.57 eV and the full width at half maximum increases from 1.0 eV (SG) to 1.29 eV (Pt<sub>0.9</sub>Pd<sub>0.1</sub>/SG); hence, the broadened peak can be convoluted into another peak at 285.68 eV corresponding to the sp<sup>3</sup> C-C bond (Figure S7b, Supporting Information). The π-π\* peak is also negatively shifted from 290.65 to 289.25 eV. These differences between SG and Pt<sub>0.9</sub>Pd<sub>0.1</sub>/SG can be attributed to the interaction between the Pt d-orbital and π-π carbon in graphene.

The sulfur content of SG is 3.16 at% (Table S1, Supporting Information), mostly consisting of the thiophenic groups (Figure S7c, Supporting Information). The high-resolution sulfur signal (S2p) was deconvoluted into two major peaks located at 163.74 and 164.92 eV and two minor peaks at 165.09 and 166.27 eV. The two major peaks resulting from the S2p spin-orbit doublet of the C-S-C bond (S2p<sub>1/2</sub> at 163.74 eV and S2p<sub>3/2</sub> at 164.92 eV) were separated by 1.18 eV, which is consistent in value with the theoretical spin doublet separation of 1.13 eV.<sup>[31]</sup> The two minor peaks can be attributed to carbon bonded with SO<sub>x</sub> species (—C—SO<sub>x</sub>).<sup>[32,33]</sup> Thiophene species incorporate with graphene in a pentagonal configuration, therefore residing at the edge and defected sites of SG. Therefore, sulfur in SG can serve as a platform for anchoring nucleation and growth of Pt ions.<sup>[10]</sup> In addition to sulfur peak analysis, the fitted Pt 4f<sub>7/2</sub> and Pt 4f<sub>5/2</sub> peaks for Pt<sub>0.9</sub>Pd<sub>0.1</sub>/SG are observed at 71.23 and 74.56 eV, respectively (Figure S7d, Supporting Information), while those for Pt<sub>0.5</sub>Pd<sub>0.5</sub>/SG (50–50% Pt and Pd) are observed at 71.34 and 74.67 eV, respectively (Figure S7e, Supporting Information). The shift in peaks of 0.11 eV can be attributed to the interaction of Pt and the support material. This is further supported by the positive shift of 0.09 eV of S2p peak from SG to Pt<sub>0.9</sub>Pd<sub>0.1</sub>/SG (Figure S5f, Supporting Information). It has been previously demonstrated that the interaction of deposited metal on support material plays a vital role in the stability of supported catalysts.<sup>[34]</sup> The shifting in peaks can be attributed to the sulfur bonding directly with the carbon atoms in the heterocyclic configuration.<sup>[35,36]</sup>

To investigate activity and durability, ORR kinetics and accelerated durability testing (ADT) was performed using a rotating disc electrode to imitate the harsh, corrosive, and potentiodynamic states encountered at the cathode of PEMFCs. Figure 3a–c shows cyclic voltammograms of Pt<sub>0.9</sub>Pd<sub>0.1</sub>/SG and Pt<sub>0.5</sub>Pd<sub>0.5</sub>/SG catalysts together with commercial Pt/C (TKK, 28.8 wt% Pt). The cyclic voltammograms were performed in N<sub>2</sub>-saturated 0.1 M HClO<sub>4</sub> solution at a sweep rate of 50 mV s<sup>-1</sup> in the potential range of 0.05–1.20 V versus a reversible hydrogen electrode (RHE) at room temperature. This range was selected considering Pt dissolution (and subsequent agglomeration) can occur above 0.8 V versus RHE and carbon corrosion occurs above 0.9 V versus RHE.<sup>[37–39]</sup> The ECSA of the catalysts was calculated from the charge associated with the hydrogen desorption peak and normalized with the Pt mass. Before ADT, the specific ECSA of Pt<sub>0.9</sub>Pd<sub>0.1</sub>/SG and Pt<sub>0.5</sub>Pd<sub>0.5</sub>/SG are 76 and 72 m<sup>2</sup> g<sup>-1</sup><sub>Pt</sub>, respectively, which are higher in comparison to the commercial Pt/C (65 m<sup>2</sup> g<sup>-1</sup><sub>Pt</sub>) (Figure 3g). Therefore, the fact that Pt-PdNF/SG possesses higher specific ECSA despite 3–4 times larger particle sizes in comparison to commercial Pt/C nanoparticles (2–5 nm) supports the claim that the dispersion of active Pt surfaces can be improved with larger particles. In this case, the high ECSA of Pt-PdNF/SG can be attributed to its 2D core-shell nanoflower morphology, which includes higher dispersion of the catalyst, planar, and porous catalyst morphology and seamless contact between the catalyst and the SG support material. The very small changes in hydrogen adsorption and desorption peaks during ADT and the lack of large oxidative currents at potentials above 1.0 V versus RHE indicate that sulfur oxides released from SG do not have a negative effect on the synthesized materials.<sup>[40]</sup> For reference, CV behavior and ORR activity of Pd/SG was also investigated (Figure S8, Supporting Information) to show that Pd alone is not sufficient to achieve high electrochemical activity toward ORR. Comparing the double layer capacitance regions of the CV curves before ADT, both Pt-Pd/SG catalysts display higher double layer thickness in comparison to Pt/C. It is well known that electrochemical double layer capacitance is affected by the specific surface area, pore structures, and surface activity of the support materials. Graphene-based materials possess large surface area and higher capacitance capabilities, and these phenomenon can explain the increase in double layer capacitance.<sup>[4,8,9]</sup> After ADT, a relatively higher increase of the double-layer capacity under the CV curves was observed for Pt<sub>0.5</sub>Pd<sub>0.5</sub>/SG (Figure 3b) in comparison to Pt<sub>0.9</sub>Pd<sub>0.1</sub>/SG (Figure 3a). Pt<sub>0.5</sub>Pd<sub>0.5</sub>/SG undergoes more leaching away of Pd compared to the Pt<sub>0.9</sub>Pd<sub>0.1</sub>/SG due to the higher initial presence of Pd. This results in higher exposed surface area of highly porous SG, leading to enhanced double layer capacitance.

The ORR polarization curves of the catalysts are shown in Figure 3d–f. The ORR curves were recorded at room temperature in an O<sub>2</sub>-saturated 0.1 M HClO<sub>4</sub> solution. The kinetic current for each ORR polarization curve was calculated using the Koutecký-Levich equation and normalized against Pt mass and ECSA for mass and specific activities ( $j_{k,\text{mass}}$  and  $j_{k,\text{specific}}$ ), respectively. Before ADT, the mass and specific activities of Pt<sub>0.9</sub>Pd<sub>0.1</sub>/SG and Pt<sub>0.5</sub>Pd<sub>0.5</sub>/SG are significantly improved in the 0.86–0.94 V versus RHE region relative to Pt/C. At 0.9 V versus RHE, the mass activities of Pt<sub>0.9</sub>Pd<sub>0.1</sub>/SG and



**Figure 3.** Cyclic voltammetry curves for a) Pt<sub>0.9</sub>Pd<sub>0.1</sub>/SG, b) Pt<sub>0.5</sub>Pd<sub>0.5</sub>/SG, and c) Pt/C before and 3000 cycles. ORR polarization curve of d) Pt<sub>0.9</sub>Pd<sub>0.1</sub>/SG, e) Pt<sub>0.5</sub>Pd<sub>0.5</sub>/SG, and f) Pt/C before and after 3000 cycles. g) ECSA, h) mass activity, and i) specific activity bar chart of Pt<sub>0.9</sub>Pd<sub>0.1</sub>/SG, Pt<sub>0.5</sub>Pd<sub>0.5</sub>/SG, and Pt/C before and after 3000 cycles. j) CV curves. k) ORR polarization curves. l) Bar chart comparing ECSA, mass activity, and specific activity of Pt<sub>0.9</sub>Pd<sub>0.5</sub>/SG with commercial Pt/C before and after 10 000 cycles.

Pt<sub>0.5</sub>Pd<sub>0.5</sub>/SG are 371 and 115 mA mg<sup>-1</sup> Pt<sup>b</sup>, respectively, with the former representing a 3.12-fold improvement over commercial Pt/C (119 mA mg<sup>-1</sup> Pt<sup>b</sup>) (Figure 3h). The specific activities at 0.9 V versus RHE for Pt<sub>0.9</sub>Pd<sub>0.1</sub>/SG and Pt<sub>0.5</sub>Pd<sub>0.5</sub>/SG are 0.491 and 0.197 mA cm<sup>-2</sup> Pt<sup>b</sup>, respectively, with the former representing a 2.71-fold increase over commercial Pt/C (0.183 mA cm<sup>-2</sup> Pt<sup>b</sup>) (Figure 3i). The high activities and ECSA of Pt<sub>0.9</sub>Pd<sub>0.1</sub>/SG could be attributed to the higher exposure of the (111) facets of Pt, which has comparatively better activity than the (100) facet and core–shell structure.<sup>[41–43]</sup> The addition of Pd to the core–shell

structure also lowers its d-band center energy,<sup>[44]</sup> which provides a weaker Pt–OH<sub>ads</sub> interaction<sup>[45,46]</sup> and leads to a decrease in –OH coverage at a given potential and a resulting increase in the number of sites available for O<sub>2</sub> adsorption, dissociation, and reduction. Previous work has demonstrated that the vacant d-orbital of individual atoms play a vital role in the catalyst activity and are the basis for excellent catalytic activity.<sup>[47]</sup> The addition of another metal to the Pt downshifts its d-band center and therefore reduces oxygen binding energy and increases catalytic activity compared to pure Pt.<sup>[48–50]</sup> Generally, bimetallic

structures form weaker bonds with oxygen in comparison with pure Pt, as the variation in oxygen metal bond depends to a large extent on the coupling between the oxygen 2p states and metal 3d states. This leads to a lower position of the d-band center relative to the Fermi level, which affects the metal–oxygen bond interaction and thus benefits ORR activity.<sup>[49]</sup> In the case of Pt<sub>0.9</sub>Pd<sub>0.1</sub>/SG, although the thickness of the Pt shell is relatively high, defects in the core–shell structure can allow for sites where Pd atoms modify the electronic structure of the Pt surface. Moreover, the high mass and specific activity of Pt<sub>0.9</sub>Pd<sub>0.1</sub>/SG could be associated to its nanoflower morphology, with its well-attached 2D structure providing improved electron transfer kinetics.

The electrocatalytic durability of the catalysts was evaluated through accelerated tests applying linear potential sweeps in the range of 0.05–1.2 V versus RHE at a rate of 50 mV s<sup>-1</sup> in an N<sub>2</sub> saturation 0.1 M HClO<sub>4</sub> solution at room temperature. After 3000 ADT cycles, Pt<sub>0.9</sub>Pd<sub>0.1</sub>/SG retains most of its ECSA and ORR activity. The ECSA of Pt<sub>0.9</sub>Pd<sub>0.1</sub>/SG, Pt<sub>0.5</sub>Pd<sub>0.5</sub>/SG, and Pt/C after 3000 cycles was 72, 45, and 43 m<sup>2</sup> g<sup>-1</sup><sub>Pt</sub> (Figure 3g), representing decreases of 5, 38, and 34%, respectively. In terms of catalytic durability after 3000 cycles, the Pt<sub>0.9</sub>Pd<sub>0.1</sub>/SG only exhibits a 20% loss in mass activity (297 mA mg<sup>-1</sup><sub>Pt</sub>) and 14% loss of specific activity (0.421 mA cm<sup>-2</sup>), while Pt<sub>0.5</sub>Pd<sub>0.5</sub>/SG loses 63% (42 mA mg<sup>-1</sup><sub>Pt</sub>) and 52% (0.095 mA cm<sup>-2</sup><sub>Pt</sub>) and commercial Pt/C loses 81% (23 mA mg<sup>-1</sup><sub>Pt</sub>) and 71% (0.053 mA cm<sup>-2</sup><sub>Pt</sub>) of its mass and specific activity, respectively (Figure 3h,i). Indeed, after 3000 ADT cycles, the mass and specific activities of Pt<sub>0.9</sub>Pd<sub>0.1</sub>/SG are 13 and eight times higher than commercial Pt/C, respectively. Even after 10 000 ADT cycles

under the same condition (0.05–1.2 V vs RHE) (Figure 3j–l), the specific ECSA of Pt<sub>0.9</sub>Pd<sub>0.1</sub>/SG (54 m<sup>2</sup> g<sup>-1</sup><sub>Pt</sub>) remains higher than Pt/C after 3000 cycles (43 m<sup>2</sup> g<sup>-1</sup><sub>Pt</sub>) and 10 000 cycles (39 m<sup>2</sup> g<sup>-1</sup><sub>Pt</sub>). Moreover, the mass and specific activities of Pt<sub>0.9</sub>Pd<sub>0.1</sub>/SG after 10 000 cycles (282 mA mg<sup>-1</sup><sub>Pt</sub> and 0.525 mA cm<sup>-2</sup><sub>Pt</sub>) remain higher than the initial Pt/C activity (119 mA mg<sup>-1</sup><sub>Pt</sub> and 0.183 mA cm<sup>-2</sup><sub>Pt</sub>), and are 25 and 18 times higher than the mass and specific activities of Pt/C after 10 000 cycles (11 mA mg<sup>-1</sup><sub>Pt</sub> and 0.0285 mA cm<sup>-2</sup><sub>Pt</sub>), respectively (Figure 3l). To further emphasize, Pt<sub>0.9</sub>Pd<sub>0.1</sub>/SG displays a mass activity loss of only 24% compared to the 91% mass activity loss of commercial Pt/C, which is critically important to the success of prospective ORR catalysts in PEMFCs. The durability of Pt<sub>0.9</sub>Pd<sub>0.1</sub>/SG, given the aggressive ADT potential range (0.05–1.2 V vs RHE) used in this work in comparison to other recent Pt-based catalyst reports, is particularly impressive.<sup>[18,22,51,52]</sup>

The exceptional stability of Pt<sub>0.9</sub>Pd<sub>0.1</sub>/SG is partly attributed to its high graphitic content, the core–shell nanoflower architecture of Pt–Pd, and the presence of functional anchoring groups and strong interactions between SG and Pt.<sup>[22]</sup> Additionally, the Pd core delivers long term stability to the Pt shell layer, since Pd has a lower oxidation potential (0.92 V vs RHE) than Pt (1.19 V vs RHE), therefore preventing the cathode potential reaching a value where Pt oxidation can take place.<sup>[4]</sup> Since it is difficult to synthesize a pore-free Pt shell, the Pd core will establish contact with the electrolyte and gradually oxidize when the potential rises above its oxidation potential. Oxidized Pd<sup>2+</sup> will subsequently diffuse through any pores in the Pt shell, leaving empty space in the core. After prolonged

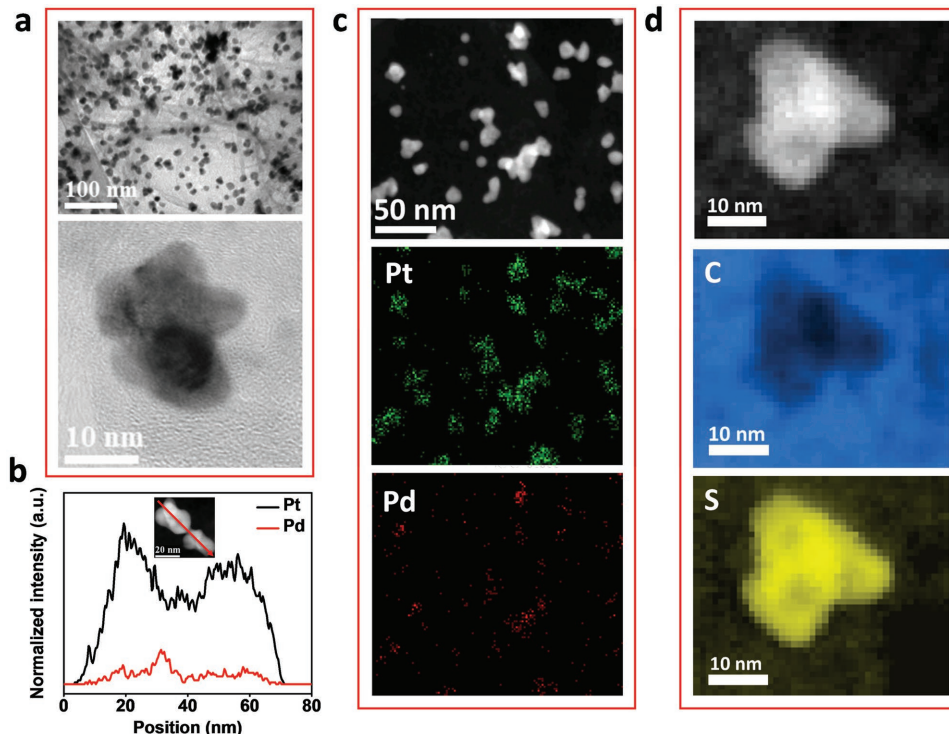


**Figure 4.** a) TEM and HR-TEM images of Pt<sub>0.9</sub>Pd<sub>0.1</sub>/SG after 10 000 cycles. b) EDX line scan profiles of Pt (black) and Pd (red) of two Pt–Pd core–shell nanoflower particles after 10 000 cycles. c) Low magnification HAADF-STEM image and corresponding EDX maps of Pt<sub>0.9</sub>Pd<sub>0.1</sub>/SG after 10 000 cycles. d) HAADF-STEM image of Pt<sub>0.9</sub>Pd<sub>0.1</sub>/SG after 10 000 cycles and corresponding EELS maps of carbon and sulfur.

potential cycling, the empty space left causes the Pt shell to undergo small contractions and become even less reactive.<sup>[44]</sup> Therefore, the Pd core increases the stability of the Pt shell by inducing lattice contractions and by acting as a sacrificial anode to provide cathodic protection to the Pt shell. Evidence of this protection mechanism is provided by postcycling TEM analysis.

After 10 000 ADT cycles,  $\text{Pt}_{0.9}\text{Pd}_{0.1}/\text{SG}$  was removed from the glassy carbon electrode by rinsing in ethanol and analyzed with TEM to search for the presence of agglomeration or dissolution of Pt particles, and any other catalyst morphological changes. The Pt–Pd particles remained well-dispersed on SG, while no significant agglomeration or overall changes in its morphology were observed (**Figure 4a**). However, in comparison to the catalyst before cycling (**Figure 2f**), the EDX line spectra in **Figure 4b** shows a clear decrease of Pd intensity relative to the Pt intensity, thus demonstrating that Pd indeed dissolves during cycling due to defects in the core–shell structure. However, it should be noted that part of Pd remains after ADT testing. This can be attributed to the parting limit, where higher atomic ratio of the more noble component (Pt in this case) diminishes dissolution of the other or both metals in a binary systems.<sup>[53]</sup> EDX elemental mapping of individual nano-flowers in  $\text{Pt}_{0.9}\text{Pd}_{0.1}/\text{SG}$  shows the retention of the Pd core–Pt shell structure after ADT (**Figure 4c**), while mapping at lower magnification shows the homogenous distribution of carbon, sulfur, Pt, and Pd is also maintained (**Figure S9**, Supporting Information). EELS elemental mapping (**Figure 4d**) shows that sulfur stays concentrated at the edge of core–shell nano-flower catalyst, indicating the interaction between sulfur and Pt remains after ADT.

In summary, we have designed and synthesized a novel ORR catalyst composed of Pt–Pd core shell nanoflower-like structures deposited on sulfur-doped graphene. The core–shell nanoflower structures exhibit a substantial enhancement in electrochemical activity and remarkable long-term stability compared with commercial Pt/C. After 3000 ADT cycles, the  $\text{Pt}_{0.9}\text{Pd}_{0.1}/\text{SG}$  catalyst retains 80 and 86% of its mass and specific activity, respectively, while Pt/C only retains 19 and 28%. Even after longer-term ADT (10 000 cycles), the mass activity of  $\text{Pt}_{0.9}\text{Pd}_{0.1}/\text{SG}$  was 2.4 times higher than the initial activity of Pt/C, demonstrating its exceptional stability. Through the combination of a unique SG support and nanostructured 2D core–shell structure, this work provides an attractive strategy for obtaining excellent catalyst performance and durability to overcome the performance barriers of traditional PEMFC cathodes electrocatalyst.

## Supporting Information

Supporting Information is available from the Wiley Online Library or from the author.

## Acknowledgements

A.M.J. and F.M.H. contributed equally to this work. This research was supported by the Natural Sciences and Engineering Research Council of Canada (NSERC). The TEM and EELS characterizations were conducted at the Canadian Center for Electron Microscopy (CCEM) at McMaster University.

## Conflict of Interest

The authors declare no conflict of interest.

## Keywords

electrocatalyst, oxygen reduction, PEMFCs, platinum

Received: November 17, 2017

Revised: December 21, 2017

Published online:

- [1] United States Department of Energy: Technical Plan – Fuel Cells, **2012**, [http://www1.eere.energy.gov/hydrogenandfuelcells/mypp/pdfs/fuel\\_cells.pdf](http://www1.eere.energy.gov/hydrogenandfuelcells/mypp/pdfs/fuel_cells.pdf) (accessed: November 2013).
- [2] J. Rossmeisl, G. S. Karlberg, T. Jaramillo, J. K. Nørskov, *Faraday Discuss.* **2008**, *140*, 337.
- [3] W. Tang, G. Henkelman, *J. Chem. Phys.* **2009**, *130*, 194504.
- [4] M. A. Hoque, F. M. Hassan, D. Higgins, J.-Y. Choi, M. Pritzker, S. Knights, S. Ye, Z. Chen, *Adv. Mater.* **2015**, *27*, 1229.
- [5] K. Sasaki, H. Naohara, Y. Cai, Y. M. Choi, P. Liu, M. B. Vukmirovic, J. X. Wang, R. R. Adzic, *Angew. Chem., Int. Ed. Engl.* **2010**, *49*, 8602.
- [6] Z. Chen, M. Waje, W. Li, Y. Yan, *Angew. Chem., Int. Ed. Engl.* **2007**, *46*, 4060.
- [7] C. Koenigsmann, A. C. Santulli, K. Gong, M. B. Vukmirovic, W. P. Zhou, E. Sutter, S. S. Wong, R. R. Adzic, *J. Am. Chem. Soc.* **2011**, *133*, 9783.
- [8] B. Y. Xia, W. T. Ng, H. Bin Wu, X. Wang, X. W. D. Lou, *Angew. Chem., Int. Ed. Engl.* **2012**, *51*, 7213.
- [9] N. S. Porter, H. Wu, Z. Quan, J. Fang, *Acc. Chem. Res.* **2013**, *46*, 1867.
- [10] S. J. Guo, S. Zhang, D. Su, S. H. Sun, *J. Am. Chem. Soc.* **2013**, *135*, 13879.
- [11] R. Wang, D. C. Higgins, M. A. Hoque, D. Lee, F. Hassan, Z. Chen, *Sci. Rep.* **2013**, *3*, 1.
- [12] S. Sun, G. Zhang, D. Geng, Y. Chen, R. Li, M. Cai, X. Sun, *Angew. Chem., Int. Ed.* **2011**, *50*, 422.
- [13] Y. Zhou, K. Neyerlin, T. S. Olson, S. Pylypenko, J. Bult, H. N. Dinh, T. Gennett, Z. Shao, R. O'Hare, *Energy Environ. Sci.* **2010**, *3*, 1437.
- [14] S. Sun, G. Zhang, D. Geng, Y. Chen, M. N. Banis, R. Li, M. Cai, X. Sun, *Chemistry* **2010**, *16*, 829.
- [15] Y. Shao, J. Sui, G. Yin, Y. Gao, *Appl. Catal., B* **2008**, *79*, 89.
- [16] L. Zhang, S. Zhu, Q. Chang, D. Su, J. Yue, Z. Du, M. Shao, *ACS Catal.* **2016**, *6*, 3428.
- [17] D. Wang, Y. Yu, J. Zhu, S. Liu, D. A. Muller, H. D. Abruña, *Nano Lett.* **2015**, *15*, 1343.
- [18] X. Wang, S.-I. Choi, L. T. Roling, M. Luo, C. Ma, L. Zhang, M. Chi, J. Liu, Z. Xie, J. A. Herron, M. Mavrikakis, Y. Xia, *Nat. Commun.* **2015**, *6*, 7594.
- [19] D. Higgins, M. A. Hoque, M. H. Seo, R. Wang, F. Hassan, J.-Y. Choi, M. Pritzker, A. Yu, J. Zhang, Z. Chen, *Adv. Funct. Mater.* Butterworth-Heinemann **2014**, *24*, 4325.
- [20] J. W. Mullin, *Crystallization*, Elsevier, **2001**, pp. 216–288.
- [21] F. Fievet, J. P. Lagier, M. Figlarz, *MRS Bull.* **1989**, *14*, 29.
- [22] Y. Xiong, Y. Xia, *Adv. Mater.* **2007**, *19*, 3385.
- [23] I. Herrmann, U. I. Kramm, J. Radnik, S. Fiechter, P. Bogdanoff, *J. Electrochem. Soc.* **2009**, *156*, B1283.
- [24] J. Liang, X. Du, C. Gibson, X. W. Du, S. Z. Qiao, *Adv. Mater.* **2013**, *25*, 6226.
- [25] S. Yang, L. Zhi, K. Tang, X. Feng, J. Maier, K. Müllen, *Adv. Funct. Mater.* **2012**, *22*, 3634.

- [26] S. Shrestha, Y. Liu, W. E. Mustain, *Catal. Rev.: Sci. Eng.* **2011**, *53*, 256.
- [27] X. H. Yang, J. W. Guo, S. Yang, Y. Hou, B. Zhang, H. G. Yang, *J. Mater. Chem. A* **2014**, *2*, 614.
- [28] S. A. Best, P. Brant, R. D. Feltham, T. B. Rauchfuss, D. M. Roundhill, R. A. Walton, *Inorg. Chem.* **1977**, *16*, 1976.
- [29] N. A. Travlou, G. Z. Kyzas, N. K. Lazaridis, E. A. Deliyanni, *Langmuir* **2013**, *29*, 1657.
- [30] T. I. T. Okpalugo, P. Papakonstantinou, H. Murphy, J. McLaughlin, N. M. D. Brown, *Carbon* **2005**, *43*, 153.
- [31] A. Barrie, I. W. Drummond, Q. C. Herd, *J. Electron Spectrosc. Relat. Phenom.* **1974**, *5*, 217.
- [32] C. H. Choi, S. H. Park, S. I. Woo, *Green Chem.* **2011**, *13*, 406.
- [33] Z. Liu, H. Nie, Z. Yang, J. Zhang, Z. Jin, Y. Lu, Z. Xiao, S. Huang, *Nanoscale* **2013**, *5*, 3283.
- [34] B. Qiao, J.-X. Liang, A. Wang, C.-Q. Xu, J. Li, T. Zhang, J. J. Liu, *Nano Res.* **2015**, *8*, 2913.
- [35] M. E. Labib, J. H. Thomas, D. D. Embert, *Carbon* **1984**, *22*, 445.
- [36] Y. Chang, F. Hong, C. He, Q. Zhang, J. Liu, *Adv. Mater.* **2013**, *25*, 4794.
- [37] Y. Shao-Horn, W. C. Sheng, S. Chen, P. J. Ferreira, E. F. Holby, D. Morgan, *Top. Catal.* **2007**, *46*, 285.
- [38] H. A. Gasteiger, S. S. Kocha, B. Sompalli, F. T. Wagner, *Appl. Catal., B* **2005**, *56*, 9.
- [39] P. J. Ferreira, G. J. la O', Y. Shao-Horn, D. Morgan, R. Makharia, S. Kocha, H. A. Gasteiger, *J. Electrochem. Soc.* **2005**, *152*, A2256.
- [40] J. Fu, M. Hou, C. Du, Z. Shao, B. Yi, *J. Power Sources* **2009**, *187*, 32.
- [41] D. F. van der Vliet, C. Wang, D. Tripkovic, D. Strmcnik, X. F. Zhang, M. K. Debe, R. T. Atanasoski, N. M. Markovic, V. R. Stamenkovic, *Nat. Mater.* **2012**, *11*, 1051.
- [42] N. Markovic, *J. Electrochem. Soc.* **1997**, *144*, 1591.
- [43] J. Zhang, M. B. Vukmirovic, Y. Xu, M. Mavrikakis, R. R. Adzic, *Angew. Chem., Int. Ed.* **2005**, *44*, 2132.
- [44] M. B. Vukmirovic, J. Zhang, K. Sasaki, A. U. Nilekar, F. Uribe, M. Mavrikakis, R. R. Adzic, *Electrochim. Acta* **2007**, *52*, 2257.
- [45] J. X. Wang, J. Zhang, R. R. Adzic, *J. Phys. Chem. A* **2007**, *111*, 12702.
- [46] A. U. Nilekar, M. Mavrikakis, *Surf. Sci.* **2008**, *602*, L89.
- [47] P. Hu, Z. Huang, Z. Amghous, M. Makkee, F. Xu, F. Kapteijn, A. Dikhtiarenko, Y. Chen, X. Gu, X. Tang, *Angew. Chem., Int. Ed.* **2014**, *53*, 3418.
- [48] V. Stamenkovic, B. S. Mun, K. J. J. Mayrhofer, P. N. Ross, N. M. Markovic, J. Rossmeisl, J. Greeley, J. K. Nørskov, *Angew. Chem., Int. Ed.* **2006**, *45*, 2897.
- [49] V. R. Stamenkovic, B. S. Mun, M. Arenz, K. J. J. Mayrhofer, C. A. Lucas, G. Wang, P. N. Ross, N. M. Markovic, *Nat. Mater.* **2007**, *6*, 241.
- [50] J. Greeley, I. E. L. Stephens, A. S. Bondarenko, T. P. Johansson, H. A. Hansen, T. F. Jaramillo, J. Rossmeisl, I. Chorkendorff, J. K. Nørskov, *Nat. Chem.* **2009**, *1*, 552.
- [51] M. A. Hoque, F. M. Hassan, M.-H. Seo, J.-Y. Choi, M. Pritzker, S. Knights, S. Ye, Z. Chen, *Nano Energy* **2016**, *19*, 27.
- [52] J. Hu, L. Wu, K. A. Kuttyiel, K. R. Goodman, C. Zhang, Y. Zhu, M. B. Vukmirovic, M. G. White, K. Sasaki, R. R. Adzic, *J. Am. Chem. Soc.* **2016**, *138*, 9294.
- [53] R. Newman, S. Corcoran, J. Erlebacher, M. J. Aziz, K. Sieradzki, *MRS Bull.* **1999**, *24*, 24.